KYBERNETIKA — VOLUME *56* (2020), NUMBER 4, PAGES 821–841

# A GENERALISED PROPORTIONAL-DERIVATIVE FORCE/VISION CONTROLLER FOR TORQUE-DRIVEN PLANAR ROBOTIC MANIPULATORS

Carlos Vidrios-Serrano, Marco Mendoza, Isela Bonilla and Berenice Maldonado-Fregoso

In this paper, a family of hybrid control algorithms is presented; where it is merged a free camera-calibration image-based control scheme and a direct force controller, both with the same priority level. The aim of this generalised hybrid controller is to regulate the robot-environment interaction into a two-dimensional task-space. The design of the proposed control structure takes into account most of the dynamic effects present in robot manipulators whose inputs are torque signals. As examples of this generalised structure of hybrid force/vision controllers, a linear proportional-derivative structure and a nonlinear proportional-derivative one (based on the hyperbolic tangent function) are presented. The corresponding stability analysis, using Lyapunov's direct method and invariance theory, is performed to proof the asymptotic stability of the equilibrium vector of the closed-loop system. Experimental tests of the control scheme are presented and a suitable performance is observed in all the cases. Unlike most of the previously presented hybrid schemes, the control structure proposed herein achieves soft contact forces without overshoots, fast convergence of force and position error signals, robustness of the controller in the face of some uncertainties (such as camera rotation), and safe operation of the robot actuators when saturating functions (non-linear case) are used in the mathematical structure. This is one of the first works to propose a generalized structure of hybrid force/vision control that includes a closed loop stability analysis for torque-driven robot manipulators.

*Keywords:* control, force, vision, robot manipulator, stability

*Classification:* 68T40, 93C85, 93D05

## 1. INTRODUCTION

Over the years, the robotic tasks have been evolving into more complex areas and this causes that robotic systems require of different kind of sensors, as a way to obtain information of their surroundings and their own condition [1, 18, 24, 27, 28, 29]. Particularly, robotic systems that work in unstructured environments require information that allows them to navigate and interact with the environment. Cameras have been one of the main sensors that have been used in these cases due to the large volume of information

DOI: 10.14736/kyb-2020-4-0821

that can be obtained by processing the images. The vision-based robot control is also known as visual servoing [10].

In recent years different types of applications have emerged using computer vision. For example, [22] present a computer vision system used to estimate the kinematic configuration of a robot and detect robot-environment interaction without proprioceptive sensors. The assembly robots represent another task where computer vision systems are commonly used [9, 20]. Furthermore, some complex data can be estimated by vision systems, as in [16], where a control algorithm is proposed in order to cut deformable objects and a vision system is used in order to estimate the deformation and proportionally adjust the control signals.

On the other hand, if a robot is to interact with its environment in a safe way, it is important to use force/torque sensors and an adequate control algorithm in order to regulate this interaction. Some examples of control algorithms for robot-environment interaction tasks are presented in [4], as a direct force regulator, or in [6, 26], as a hybrid force/position controller. On the other hand, indirect force controllers are presented in [5], based on the stiffness of the environment, or in [8, 13], based on the mechanical impedance that characterizes such interaction.

Now, when combining or merging information coming from force/torque sensors and vision systems into the same control structure, some technical difficulties arise because of the different kind of data from each sensor. In order to address this problem, several force/vision control schemes have been proposed in the literature, where both type of information are fused: [21] propose a hybrid scheme where a force controller is mixed with a vision-based control algorithm, which has as limitation that the orthogonality of the position and force components must be assured, in order to obtain a good performance; therefore, this controller has as disadvantage that force component can not influence on the position one (visual) and vice versa, in consequence, each controller tries to achieve its own goal regardless of whether the other one reach its. Another approach of force/vision control is presented by [2], where a vision-based control algorithm is used in order to estimate a target position for the robot end effector, and once the robot is close enough, the system switches to a force controller to complete the interaction task. Therefore, in order to achieve a suitable performance, an accurate estimate of the target is required, otherwise the end effector may not reach the target and, once the change to force control mode has been made, it is not possible to obtain a new estimate because the vision system is turned off.

Other methods that allow to combine visual and force information into a robot control scheme are based on the impedance approach, such as those presented in [3, 19]. The main drawback of this technique, according to a study presented in [17], is that local minima may occur under certain conditions and cause oscillations in the position and interaction force of the robot. [17] propose an external force/vision control algorithm, where the force signal proportionally modify the target position and then, the controller tries to reach the goal force and a virtually modified desired position; therefore, in this hybrid control algorithm, force component has higher priority than the visual one. In general, interaction and vision-based control schemes operate in the Cartesian space, and one of the most relevant methods that serves as the basis of our proposal is the energy shaping methodology [25], which is a method for task-oriented coordinate control

applicable even when holonomic constraints are added to the system.

Another restrictive feature of vision-based robot controllers is the difference between the sample rate of a vision system (typically between 20 to 30 frames per second (fps)) and the sample rate of the robot hardware (typically up to 1 kHz), causing that for some periods of time the robot operates in blind mode. In order to minimize the effects of these blind periods, some estimation methods have been integrated into vision systems. Kalman filter is a suitable estimation tool used in [14, 23] and its applications range from filtering noisy signals to estimating the pose of robot when an occlusion occurs in the vision system [15].

The vast majority of the papers presented in the literature that address this issue are focused on kinematic control schemes or do not include a stability analysis. This paper presents the proposal of a family of controllers that combines the main features of the vision-based control proposed by [11] and the force regulator presented by [4]. The proposed control scheme is a torque-based control scheme (dynamic control) with a hybrid structure that merges visual and force information at the same level of priority, where a direct force controller and a free camera-calibration image-based visual scheme are combined in order to control a non-redundant robot. As a theoretical support of the proposed scheme, a full stability analysis in the Lyapunov sense was performed and the asymptotic stability of the closed-loop equilibrium vector is demonstrated. To illustrate the generality of the proposed control structure, two particular cases are presented: the first one is a linear proportional-derivative controller and the second is a nonlinear proportional-derivative controller based on the hyperbolic tangent function (tanh). Finally, experimental results for both study cases are presented, where a good performance of both controllers is observed. Additionally, it is important to note that a video camera with a sampling frequency up to 200 fps was used for experimental evaluation, therefore an estimation method like Kalman filter was not required.

## 2. SYSTEM MODEL

The dynamic model of a robot of $n$ degrees of freedom, interacting with the environment into the $m$-dimensional Cartesian space, is described by

$$M(q)\ddot{q} + C(q,\dot{q})\dot{q} + g(q) + B\dot{q} = \tau - J^T(q)f_e \tag{1}$$

where $q \in \mathbb{R}^n$ is the vector of joint positions, $\dot{q} \in \mathbb{R}^n$ is the vector of joint velocities, $\ddot{q} \in \mathbb{R}^n$ is the vector of joint accelerations, $M(q) \in \mathbb{R}^{n\times n}$ is the symmetric and positive definite inertia matrix, $C(q,\dot{q}) \in \mathbb{R}^{n\times n}$ is the centripetal and Coriolis matrix, $B \in \mathbb{R}^{n\times n}$ is a positive definite constant diagonal matrix, whose entries $b_i > 0$, $i = 1,\ldots,n$ are the viscous friction coefficients, and $g(q) \in \mathbb{R}^n$ is the vector of gravitational torques. Additionally, $\tau \in \mathbb{R}^n$ is the vector of control torques, $J(q) \in \mathbb{R}^{m\times n}$ represents the analytical Jacobian matrix [12] and $f_e \in \mathbb{R}^m$ denotes the vector of robot-environment interaction forces [4].

Because the robot-environment interaction occurs in the task-space (Cartesian coordinates), the following forward kinematic maps are considered

$$x = f(q) \tag{2}$$
$$\dot{x} = J(q)\dot{q} \tag{3}$$
$$\ddot{x} = \dot{J}(q,\dot{q})\dot{q} + J(q)\ddot{q} \tag{4}$$

where $x$, $\dot{x}$, $\ddot{x} \in \mathbb{R}^m$ represent the vectors of position, velocity and acceleration of the end effector, respectively. While $J(q) = \partial f(q)/\partial q$ and $\dot{J}(q,\dot{q}) = dJ(q)/dt$. Moreover, the relationship between the forces $f_x \in \mathbb{R}^m$ applied to the end effector and the joint torques $\tau$ is given by [25]

$$\tau = J^T(q) f_x. \tag{5}$$

Therefore, the dynamic model (1) can be represented in task-space as

$$M_x\ddot{x} + C_x\dot{x} + g_x + B_x\dot{x} = f_x - f_e \tag{6}$$

where

$$M_x = [J^{-1}(q)]^T M(q) J^{-1}(q) \tag{7}$$
$$C_x = \left\{[J^{-1}(q)]^T C(q,\dot{q}) - M_x\dot{J}(q,\dot{q})\right\} J^{-1}(q) \tag{8}$$
$$g_x = [J^{-1}(q)]^T g(q) \tag{9}$$
$$B_x = [J^{-1}(q)]^T B J^{-1}(q). \tag{10}$$

Thus, the task-space dynamic model (6) is valid only if the robot is away from kinematic singularities (i. e. $\text{rank}(J(q)) = n$).

The following properties of the dynamic model (6) are important for the further analysis [4].

**Property 2.1.** The matrix $M_x$ is symmetric and positive definite

$$M_x > 0, \qquad M_x = M_x^T. \tag{11}$$

**Property 2.2.** Since $\dot{M}_x = C_x + C_x^T$, the matrix $\dot{M}_x - 2C_x$ is skew-symmetric, i. e.

$$\frac{1}{2}\dot{x}^T\left[\dot{M}_x - 2C_x\right]\dot{x} \equiv 0. \tag{12}$$

**Property 2.3.** The matrix $B_x$ is diagonal and positive definite

$$B_x > 0, \qquad B_x = B_x^T. \tag{13}$$

**Assumption 2.4.** Without loss of generality and because of the restrictions imposed by the vision system, a non-redundant robot and a planar task-space are considered, i. e. $m = n = 2$.

As usual in any visual servoing system, it is important to define the camera model that captures the scene; in this case, a *pin-hole* camera model in *eye-on-hand* configuration

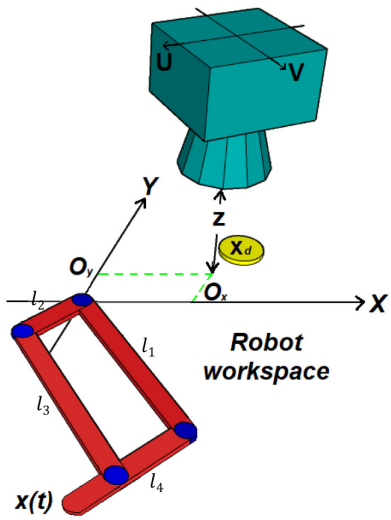


**Fig. 1.** Configuration of the visual servoing system.

is considered [7, 10], where the image plane and the robot task-space are parallel, as it is depicted in Figure 1.

For this camera model, any task-space point $P$ is projected on the image-space as [11],

$$\begin{bmatrix} p_u \\ p_v \end{bmatrix} = \alpha h R(\theta) \left\{ \begin{bmatrix} p_x \\ p_y \end{bmatrix} - \begin{bmatrix} O_x \\ O_y \end{bmatrix} \right\} + \begin{bmatrix} c_u \\ c_v \end{bmatrix} \tag{14}$$

where $[p_x\ p_y]^T$ are the coordinates of $P$, $[O_x\ O_y]^T$ is the intersection between the optical axis and the robot task-space, the vector $[c_u\ c_v]^T$ represents the image center, $\alpha$ is the scale factor (it is assumed to be negative) in pixels/m, $h$ is the magnification factor defined as

$$h \triangleq \frac{\lambda}{\lambda - z} < 0 \tag{15}$$

with $z$ being the distance between the image plane and the robot task-space, and $\lambda$ being the focal length. Finally, $R(\theta)$ is the rotation matrix generated by the clockwise rotation of the camera about its optical axis and given by

$$R(\theta) = \begin{bmatrix} \cos\theta & -\sin\theta \\ \sin\theta & \cos\theta \end{bmatrix}. \tag{16}$$

## 3. HYBRID FORCE/VISION CONTROL SCHEME

In this paper, a family of hybrid force/vision control algorithms is presented, whose control objectives are given by

$$\lim_{t\to\infty} \tilde{x}_s = 0 \tag{17}$$

$$\lim_{t\to\infty} \tilde{f} = 0. \tag{18}$$

where, according to model (14), it is possible to define $\tilde{x}_s \in \mathbb{R}^m$ as

$$\tilde{x}_s \triangleq \alpha h R(\theta)[x_d - x(t)] \tag{19}$$

with $x_d \in \mathbb{R}^m$ and $x(t)$ being the desired (constant) and current position of the end effector, respectively. While, $\tilde{f} \in \mathbb{R}^m$ is defined as

$$\tilde{f} \triangleq f_d - f_e(t) \tag{20}$$

with $f_d \in \mathbb{R}^m$ and $f_e(t)$ being the desired (constant) and current force applied to the end effector, respectively.

In order to model the robot-environment interaction according to Hooke's law of elasticity, the current force can be calculated as

$$f_e(t) = K_e[x(t) - x_e] \tag{21}$$

where $K_e = \text{diag}\,[k_{e1}, \ldots, k_{em}]$, with $k_{ej} > 0$, $j = 1, \ldots, m$, represents the stiffness matrix and $x_e \in \mathbb{R}^m$ is the location of the environment into the robot task-space [5].

In order to achieve the control objectives stated in (17) – (18), our proposal is a generalised version of the energy shaping methodology [25] with the following proportional-derivative structure

$$f_x = \nabla \mathcal{U}_{pf}\left(K_{pf}, \tilde{f}\right) + R^T(\theta)\nabla \mathcal{U}_{pv}\left(K_{pv}, \tilde{x}_s\right) - f_v\left(K_d, \dot{x}\right) + g_x + f_e \tag{22}$$

with $\nabla \mathcal{U}_{pf}\left(K_{pf}, \tilde{f}\right) \in \mathbb{R}^m$ and $\nabla \mathcal{U}_{pv}\left(K_{pv}, \tilde{x}_s\right) \in \mathbb{R}^m$ representing the gradients of artificial potential energy functions of force and position (vision), respectively, where $K_{pf} = \text{diag}\,[k_{pf1}, \ldots, k_{pfm}]$, $K_{pv} = \text{diag}\,[k_{pv1}, \ldots, k_{pvm}]$, with $k_{pfj} > 0$, $k_{pvj} > 0$, $j = 1, \ldots, m$, are matrices of proportional gains; and both functions satisfy

$$\mathcal{U}_p\left(K_p, \tilde{w}\right) > 0 \quad \forall \tilde{w} \neq 0 \tag{23}$$

$$\mathcal{U}_p\left(K_p, \tilde{w}\right) = 0 \quad \text{if } \tilde{w} = 0 \tag{24}$$

$$\tilde{w}^T \nabla \mathcal{U}_p\left(K_p, \tilde{w}\right) > 0 \quad \forall \tilde{w} \neq 0 \tag{25}$$

$$\nabla \mathcal{U}_p\left(K_p, \tilde{w}\right) = 0 \quad \text{if } \tilde{w} = 0. \tag{26}$$

While, $f_v\left(K_d, \dot{x}\right) \in \mathbb{R}^m$ represents the derivative term for energy dissipation, where $K_d = \text{diag}\,[k_{d1}, \ldots, k_{dm}]$, with $k_{dj} > 0$, $j = 1, \ldots, m$, is a matrix of derivative gains and it satisfies

$$\dot{x}^T f_v\left(K_d, \dot{x}\right) > 0 \quad \forall \dot{x} \neq 0 \tag{27}$$

$$f_v\left(K_d, \dot{x}\right) \quad = \quad 0 \quad \text{if } \dot{x} = 0. \tag{28}$$

In addition, it should be noted that the control structure uses static model-based compensation of gravitational forces and the contact forces must be measured.

By combining equations (6) and (22), it is possible to obtain the closed-loop system given by

$$M_x\ddot{x} + C_x\dot{x} + B_x\dot{x} = \nabla\mathcal{U}_{pf}\left(K_{pf}, \tilde{f}\right) + R^T(\theta)\nabla\mathcal{U}_{pv}\left(K_{pv}, \tilde{x}_s\right) - f_v\left(K_d, \dot{x}\right) \tag{29}$$

and by considering the definitions (19) – (20) and the model (21), the following state-space representation of the closed-loop system is obtained

$$\frac{d}{dt}\begin{bmatrix} \tilde{f} \\ \tilde{x}_s \\ \dot{x} \end{bmatrix} = \begin{bmatrix} -K_e\dot{x} \\ -\alpha h R(\theta)\dot{x} \\ M_x^{-1}\Psi(\tilde{f}, \tilde{x}_s, \dot{x}) \end{bmatrix} \tag{30}$$

where

$$\begin{aligned} \Psi(\tilde{f}, \tilde{x}_s, \dot{x}) \quad = \quad & \nabla\mathcal{U}_{pf}\left(K_{pf}, \tilde{f}\right) + R^T(\theta)\nabla\mathcal{U}_{pv}\left(K_{pv}, \tilde{x}_s\right) \\ & -f_v\left(K_d, \dot{x}\right) - C_x\dot{x} - B_x\dot{x}. \end{aligned} \tag{31}$$

Now, under stationary conditions, the following statements can be established.

- For the first term of equation (30),

$$\dot{\tilde{f}} = 0 \Longrightarrow -K_e\dot{x} = 0 \Longleftrightarrow \dot{x} = 0$$

  because $K_e > 0$ is a diagonal matrix, then $\exists K_e^{-1} > 0$.

- As $\dot{x} = \ddot{x} = 0$ and taking into account Property 2.1, i. e. $\exists M_x^{-1} > 0$, from the third term of the equation (30) is obtained that

$$\nabla\mathcal{U}_{pf}\left(K_{pf}, \tilde{f}\right) + R^T(\theta)\nabla\mathcal{U}_{pv}\left(K_{pv}, \tilde{x}_s\right) = 0. \tag{32}$$

Therefore, the equilibrium vector of closed-loop system (30) can be defined as

$$\begin{bmatrix} \tilde{f}_E \\ \tilde{x}_{sE} \\ \dot{x}_E \end{bmatrix} \triangleq \begin{bmatrix} f_d - f_E \\ \alpha h R(\theta)\left[x_d - x_E\right] \\ 0 \end{bmatrix} \tag{33}$$

where $f_E \in \mathbb{R}^m$ and $x_E \in \mathbb{R}^m$ are the equilibrium force and position, respectively.

Now, in order to analyze the stability of the equilibrium vector, the following Lyapunov candidate function can be considered

$$V(\tilde{f}, \tilde{x}_s, \dot{x}) = \frac{1}{2}\dot{x}^T M_x\dot{x} + \sum_{i=1}^{m}\frac{1}{k_{ei}}k_{pfi}u_{pfi}^2\left(\tilde{f}_i\right) + \frac{1}{\alpha h}\mathcal{U}_{pv}\left(K_{pv}, \tilde{x}_s\right) \tag{34}$$

where

$$\mathcal{U}_{pv}\left(K_{pv},\tilde{x}_s\right)=\left[\begin{array}{c} u_{pv1}\left(\tilde{x}_{s1}\right) \\ \vdots \\ u_{pvm}\left(\tilde{x}_{sm}\right) \end{array}\right]^T K_{pv}\left[\begin{array}{c} u_{pv1}\left(\tilde{x}_{s1}\right) \\ \vdots \\ u_{pvm}\left(\tilde{x}_{sm}\right) \end{array}\right] \tag{35}$$

and then

$$\mathcal{U}_{pf}\left(K_{pf},\tilde{f}\right)=\left[\begin{array}{c} u_{pf1}\left(\tilde{f}_1\right) \\ \vdots \\ u_{pfm}\left(\tilde{f}_m\right) \end{array}\right]^T K_{pf}\left[\begin{array}{c} u_{pf1}\left(\tilde{f}_1\right) \\ \vdots \\ u_{pfm}\left(\tilde{f}_m\right) \end{array}\right]. \tag{36}$$

The energy function (34) is positive definite, because the first term has a quadratic form and, according to Properties (23) and (24), the second and third terms are also positive definite functions.

The time derivative of function (34), along the trajectories of the closed-loop system (30), is given by

$$\begin{aligned} \dot{V}(\tilde{f},\tilde{x}_s,\dot{x}) &= \dot{x}^T M_x\ddot{x}+\frac{1}{2}\dot{x}^T\dot{M}_x\dot{x}+\nabla\mathcal{U}_{pf}^T\left(K_{pf},\tilde{f}\right)K_e^{-1}\dot{\tilde{f}} \\ &\quad +\frac{1}{\alpha h}\nabla\mathcal{U}_{pv}^T\left(K_{pv},\tilde{x}_s\right)\dot{\tilde{x}}_s \\ &= \dot{x}^T\nabla\mathcal{U}_{pf}\left(K_{pf},\tilde{f}\right)+\dot{x}^T R^T(\theta)\nabla\mathcal{U}_{pv}\left(K_{pv},\tilde{x}_s\right) \\ &\quad -\dot{x}^T f_v\left(K_d,\dot{x}\right)-\dot{x}^T C_x\dot{x}-\dot{x}^T B_x\dot{x}+\frac{1}{2}\dot{x}^T\dot{M}_x\dot{x} \\ &\quad -\nabla\mathcal{U}_{pf}^T\left(K_{pf},\tilde{f}\right)\dot{x}-\nabla\mathcal{U}_{pv}^T\left(K_{pv},\tilde{x}_s\right)R(\theta)\dot{x} \\ &= -\dot{x}^T f_v\left(K_d,\dot{x}\right)-\dot{x}^T B_x\dot{x} \end{aligned} \tag{37}$$

where $M_x\ddot{x}$, $\dot{\tilde{f}}$ and $\dot{\tilde{x}}_s$ have been replaced by the equivalent expressions from the closed-loop system (30) and Property 2.2 has been used. Then, in accordance with (27) and (13), $\dot{V}(\tilde{f},\tilde{x}_s,\dot{x})\leq 0$ and it is demonstrated that the equilibrium vector of (30) is stable in the Lyapunov sense. Moreover, LaSalle's invariance theorem [12] can be used by defining the following set

$$\begin{aligned} \Omega &= \left\{\left[\begin{array}{c}\tilde{f}\\ \tilde{x}_s\\ \dot{x}\end{array}\right]\in\mathbb{R}^{3m}:\dot{V}(\tilde{f},\tilde{x}_s,\dot{x})=0\right\} \\ &= \left\{\left[\begin{array}{c}\tilde{f}\\ \tilde{x}_s\\ 0\end{array}\right]\in\mathbb{R}^{3m}\right\}. \end{aligned} \tag{38}$$

Therefore, by the invariance theory, it is concluded that the equilibrium $(\tilde{f}_E,\tilde{x}_{sE},0)$ is asymptotically stable.

Several control algorithms arise from the generalised hybrid structure presented herein. Then, two representative study cases are described in order to show the versatility of the proposed approach.

### 3.1. Study case 1: Linear Proportional-Derivative (LPD) Hybrid Controller

A LPD hybrid controller is derived from (22) by selecting

$$u_{pfi}\left(\tilde{f}_i\right) = \frac{1}{\sqrt{2}}\tilde{f}_i \tag{39}$$

$$u_{pvi}\left(\tilde{x}_{si}\right) = \frac{1}{\sqrt{2}}\tilde{x}_{si} \tag{40}$$

for $i = 1, \ldots, m$, then

$$\nabla\mathcal{U}_{pf}\left(K_{pf}, \tilde{f}\right) = K_{pf}\tilde{f} \tag{41}$$

$$\nabla\mathcal{U}_{pv}\left(K_{pv}, \tilde{x}_s\right) = K_{pv}\tilde{x}_s \tag{42}$$

and with

$$f_v\left(K_d, \dot{x}\right) = K_d\dot{x} \tag{43}$$

the LPD force-vision controller is given by

$$f_x = K_{pf}\tilde{f} + R(\theta)^T K_{pv}\tilde{x}_s - K_d\dot{x} + g_x + f_e. \tag{44}$$

### 3.2. Study case 2: Nonlinear Proportional-Derivative (NLPD) Hybrid Controller

In order to generate a bounded structure that allows to obtain smoother control signals and according to the torque limits of the robotic system, a NLPD hybrid controller is derived from (22) by selecting

$$u_{pfi}\left(\tilde{f}_i\right) = \sqrt{\ln\left(\cosh\tilde{f}_i\right)} \tag{45}$$

$$u_{pvi}\left(\tilde{x}_{si}\right) = \sqrt{\ln\left(\cosh\tilde{x}_{si}\right)} \tag{46}$$

for $i = 1, \ldots, m$, then

$$\nabla\mathcal{U}_{pf}\left(K_{pf}, \tilde{f}\right) = K_{pf}\tanh\left(\tilde{f}\right) \tag{47}$$

$$\nabla\mathcal{U}_{pv}\left(K_{pv}, \tilde{x}_s\right) = K_{pv}\tanh\left(\tilde{x}_s\right) \tag{48}$$

and with

$$f_v\left(K_d, \dot{x}\right) = K_d\tanh\left(\dot{x}\right) \tag{49}$$

the NLPD force-vision controller is given by

$$f_x = K_{pf}\tanh\left(\tilde{f}\right) + R(\theta)^T K_{pv}\tanh\left(\tilde{x}_s\right) - K_d\tanh\left(\dot{x}\right) + g_x + f_e. \tag{50}$$

## 4. EXPERIMENTAL RESULTS

In order to evaluate the performance of the proposed hybrid control scheme, some experimental tests were carried out and the corresponding results are presented below.

The experimental setup is depicted in Figure 2 and it is composed of a four-bar, parallel drive selective compliance assembly robot arm (SCARA), a vision system and a force/torque sensor. The robot manipulator is called "Robot FC" and it was built at Robotics Laboratory of Science Faculty, Autonomous University of San Luis Potosi, Mexico. Robot FC is composed of four aluminium links and has two degrees of freedom; its active joints are actuated by two servomotors SVM-220B (SureServo$^{TM}$), with a maximum torque of 23.5 Nm and controlled in torque mode using two SVA-2300 drivers, i. e. they accept an analogue voltage as a reference torque signal.

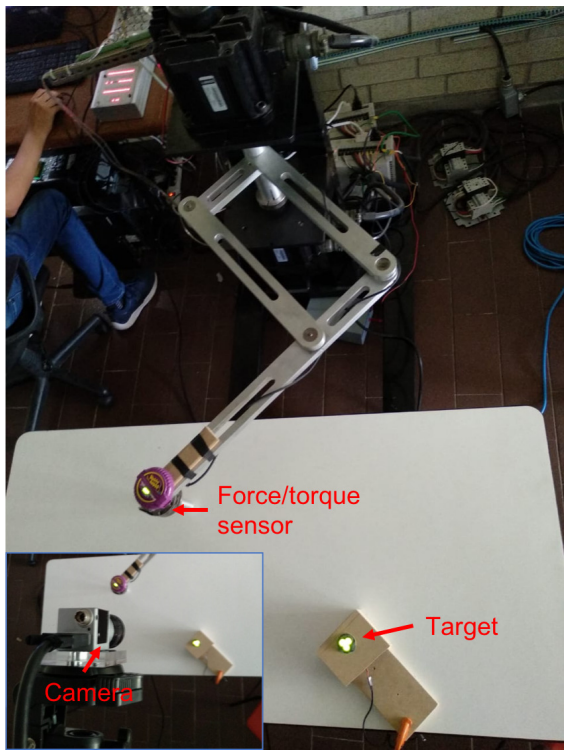


**Fig. 2.** Experimental setup.

The vision system uses an acA-1300-200uc (©Basler AG) camera with a C125-0818-5M lens of 8 mm focal length. The maximum frame rate of the camera is 200 and it can be triggered by software. For all experimental tests, the camera resolution was configured as $800 \times 600$ pixels and it was approximately placed at 1.2 meters of distance from the robot workspace and without rotation respect to the robot reference frame (a rotation angle $\theta = 0°$ was considered). It is important to highlight that neither the

distance nor the rotation of the camera was accurately measured; moreover, the location and the focal length of the camera are ignored by the controller.

On the other hand, the robot-environment interaction force was measured with a Gamma SI-130-10 six-axis force/torque sensor (©ATI Industrial Automation, Inc); only the $X$ and $Y$ axis were used, with 130 N as maximum force and 10 Nm as maximum torque in each axis, respectively.

The signal processing hardware is composed of a 2.7 GHz computer, to configure and process the visual signals, and a DS1104 board (©dSPACE Inc), to configure and process the force signals and to generate the control signals. The computer vision algorithm was written in C++ language and it consists in computing the location (centroid of a marker formed of light-emitting diodes (LEDs)) of the end-effector and the target (object with which the robot interacts); this information allows to estimate the position error $\tilde{x}_s$, which is sent to DS1104 board by RS-232 bus, with an average rate of 170 fps.

Additionally, joint position data is obtained by using incremental encoders installed in the motors, while the joint velocities are estimated from the position measurements, in order to compute $\dot{x}$ with equation (3). The reading of the data coming from the encoders, vision system and force sensor, as well as the generation of the reference voltages, are performed in the DS1104 board. The control algorithms were implemented in block diagrams using Simulink (MathWorks®) and they run in real time with a sample rate of 1.0 milliseconds on the DS1104 board.

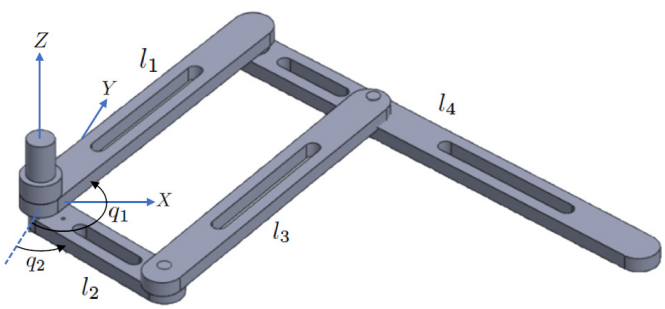


**Fig. 3.** Mechanical structure of Robot FC.

The workspace of Robot FC is a horizontal plane, therefore, the compensation of gravitational forces is not required and only the following Jacobian matrix is used

$$J(q) = \begin{pmatrix} l_1 \cos q_1 & l_4 \cos q_2 \\ l_1 \sin q_1 & l_4 \sin q_2 \end{pmatrix} \tag{51}$$

where $l_1 = 0.4191$ m. and $l_4 = 0.6096$ m. In order to prove that the Jacobian matrix (51) has not singularities, it is necessary to verify that $\det(J(q)) \neq 0$. Then, we have that

$$\det(J(q)) = l_1 l_4 \sin(q_2 - q_1) \tag{52}$$

thus $\det(J(q)) = 0$, if $q_2 - q_1 = k\pi$, $\forall k \in \mathbb{N}$. However, this case would only be possible if the links $l_1$ and $l_4$ could be aligned, which is impossible in practice by observing the

mechanical structure of the Robot FC in Figure 3, because $l_1 = l_3 > l_2$ and both ($l_1$, $l_3$) and ($l_2$, $l_4$) are parallel and coplanar.

The experimental validation consisted of performing two tests: a constrained regulation task and a point-to-point constrained path tracking. Both tests are described below.

### 4.1. Test 1: Constrained regulation task

Test 1 consisted of moving the end-effector of Robot FC from the initial location $x_s(0) = [0, 300]^T$ pixels[1] to the target position $x_{sd} = [0, 0]^T$ pixels. The target position represents the center of a cube made of MDF wood, with 10 mm of face thickness, and the marker was mounted on the cube and placed at a distance of 60 mm (approximately 76 pixels in $Y$-axis direction) from the cube edge. Therefore, the cube faces are rigid barriers that prevent reaching the target position and, according to this, the following desired interaction force is defined

$$f_d = \begin{bmatrix} 0 \\ -5 \end{bmatrix} \text{N}$$

where $f_{d1}$ and $f_{d2}$ correspond to the desired forces in the $X$-axis and $Y$-axis direction, respectively.

The experimental results of Test 1 for the LPD hybrid controller are presented in Figure 4. Controller (44) was tuned according to the procedure described in Appendix A and the gain matrices were selected as

$$\begin{aligned} K_{pf} &= \begin{bmatrix} 5 & 0 \\ 0 & 5 \end{bmatrix} \\ K_{pv} &= \begin{bmatrix} 0.5 & 0 \\ 0 & 0.1 \end{bmatrix} \\ K_d &= \begin{bmatrix} 275 & 0 \\ 0 & 275 \end{bmatrix} \end{aligned}$$

Figure 4(a) shows the behavior of the position error and it can be observed that both components try to reach zero pixels, when the robot is moving in free-space during almost 1.3 seconds. Once the contact occurs, both error components are stabilized in non-zero values ($\tilde{x}_{s1} \to 2$ pixels and $\tilde{x}_{s2} \to -75$ pixels). On the other hand, contact force components are depicted in Figure 4(b) and it can be noted that both are close to zero before the contact occurs and after, in steady state, $f_{e1} \to 0.077$ N and $f_{e2} \to -5.058$ N. Therefore, this behavior is consistent with the equilibrium point defined in equation (33), where neither the force error nor position error are equal to zero.

Additionally, in Figures 4(c) and 4(d), the applied torques and the velocity components are presented, respectively. When starting the movement of the robot, it can be observed that robot torques are close to the maximum value of 23.5 Nm, however, the movement of the robot is not influenced by this and has a smooth behavior before and

[1]According to equation (19), the position of end-effector in image plane can be defined as $x_s(t) \triangleq \alpha R(\theta) x(t)$. Additionally, according to the camera location and its focal length, the pixel-to-pixel distance is approximately 0.79 mm.

after contact. Also, the behavior of the velocity components is consistent with the task of regulation entrusted to the robot, since both are zero before starting the movement and once the steady state is reached and according to the equilibrium point defined in (33).

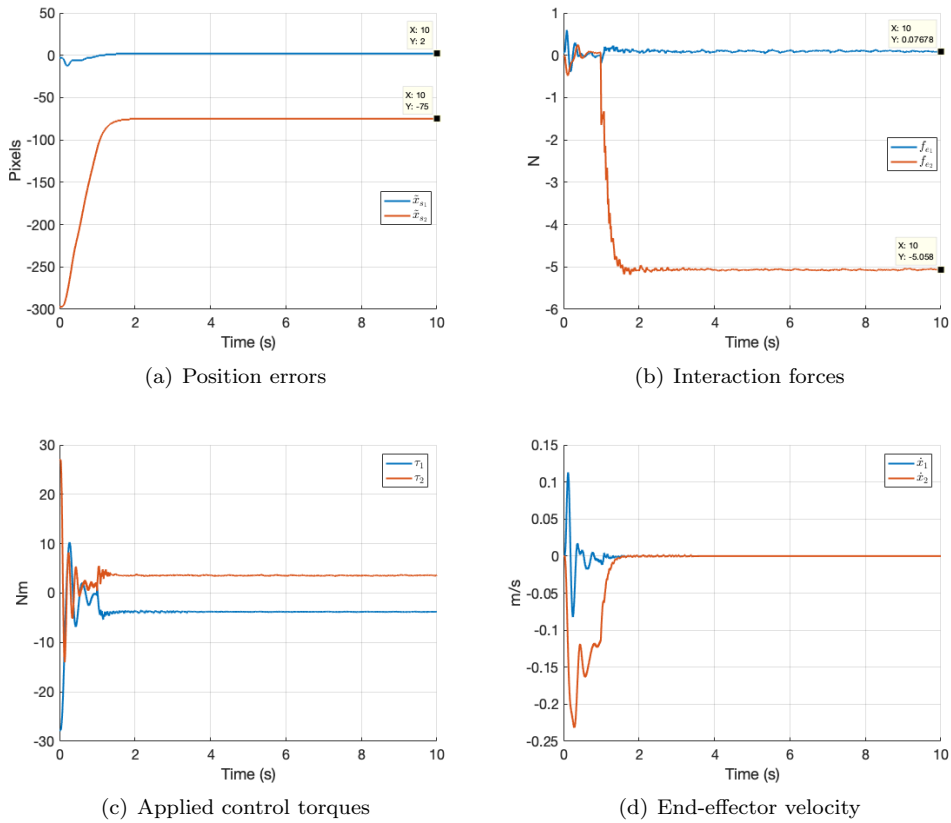


(a) Position errors

(b) Interaction forces

(c) Applied control torques

(d) End-effector velocity

**Fig. 4.** Performance of the LPD hybrid controller in Test 1.

In order to minimize the torque requirements and as a second study case, the NLPD hybrid controller (50) was implemented to perform the Test 1. According to the tuning procedure described in Appendix A, the corresponding gain matrices were selected as

$$K_{pf} = \begin{bmatrix} 10 & 0 \\ 0 & 10 \end{bmatrix}$$

$$K_{pv} = \begin{bmatrix} 5.3 & 0 \\ 0 & 5.3 \end{bmatrix}$$

$$K_{d} = \begin{bmatrix} 100 & 0 \\ 0 & 100 \end{bmatrix}$$

The results of the NLPD controller are shown in Figure 5. In a similar way, it can be observed in Figures 5(a) and 5(b) that the position and force components, respectively, are properly regulated. In steady state, the position-error components are $\tilde{x}_{s1} \to 1$ and $\tilde{x}_{s2} \to -75$ pixels, respectively, and the contact forces are $f_{e1} \to -1.12$ N and $f_{e2} \to -5.05$ N. While, the velocity components (see Figure 5(d)) tends to zero in steady state, then, the equilibrium defined in (33) is reached. Note that a force error $\tilde{f}_1 = 1.12$ N is obtained and it is caused by non-modeled interaction forces, such as the friction generated by the contact of the end effector on the surface of the wooden cube. However, in spite of this, the objective of the task continues to be met.

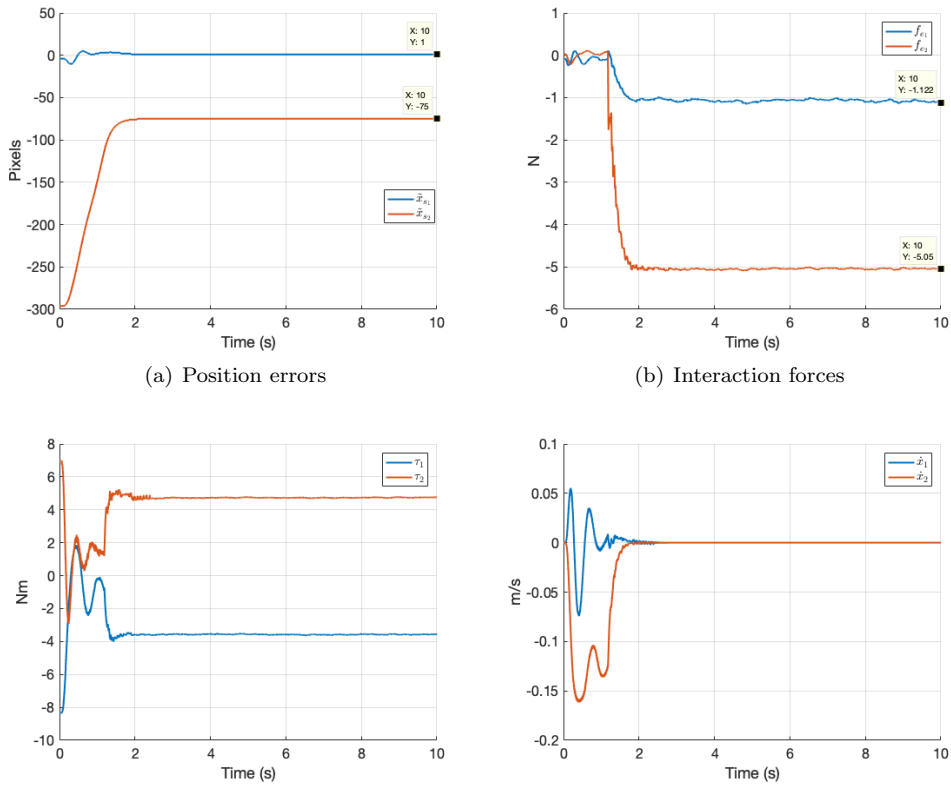


(a) Position errors

(b) Interaction forces

(c) Applied control torques

(d) End-effector velocity

**Fig. 5.** Performance of the NLPD hybrid controller in Test 1.

Furthermore, the applied torques are depicted in Figure 5(c) and it can be observed that the maximum applied torque is close to 8 Nm. Therefore, the use of saturating functions allows the robot actuators to remain working in a safe area without approaching their torque limit values.

In both study cases, it is important to highlight the smoothness of the system re-

sponse, the low speed required, as well as, no overshoots occurred during the robot-environment interaction, guaranteeing a suitable system performance.

In order to prove the robustness of the proposed control approach, Test 1 was performed again using both controllers, but rotating the camera approximately 30°. This change was unknown for both controllers and they were implemented with a rotation angle of $\theta = 0°$. The performance of both controllers was similar and, illustratively, only the results for the NLPD controller are presented in Figure 6. Again, it can be observed that the objective of the task is correctly fulfilled, by obtaining, in steady state, $\tilde{x}_{s1} \to 0$ pixels, $\tilde{x}_{s2} \to -78$ pixels, $\tilde{f}_1 \to 0.11$ N and $\tilde{f}_2 \to 0.33$ N (see Figures 6(a) and 6(b)). Finally, the torque and velocity requirements are similar to those obtained in the tests with camera rotation of 0°, as it can be observed in Figures 6(c) and 6(d).

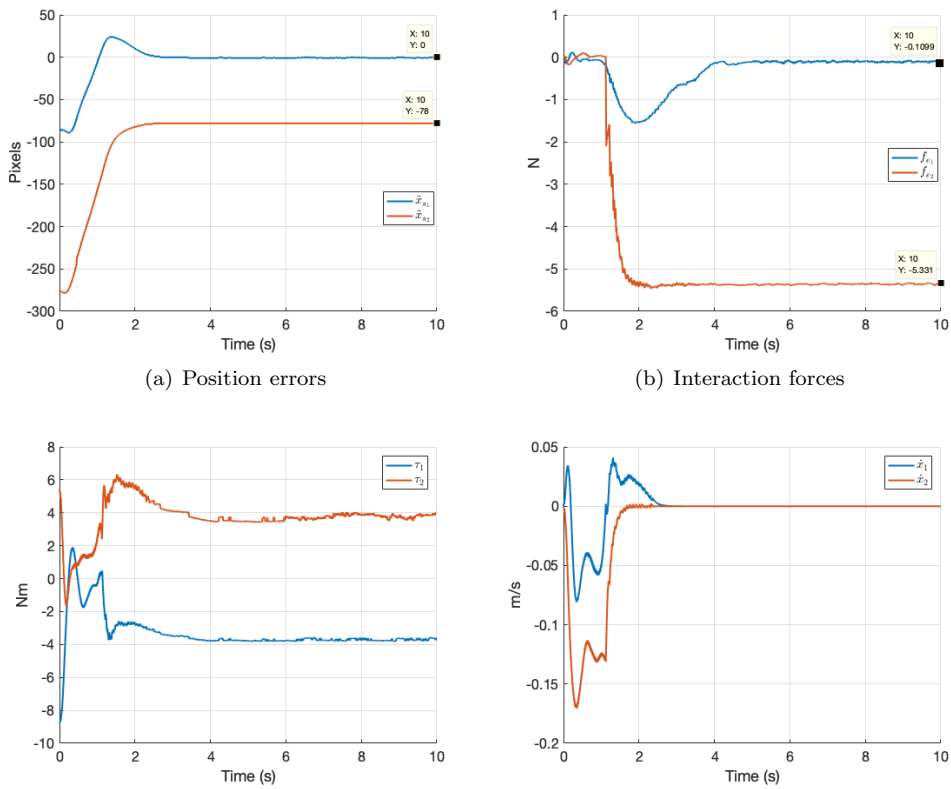


(a) Position errors

(b) Interaction forces

(c) Applied control torques

(d) End-effector velocity

**Fig. 6.** Performance of the NLPD hybrid controller in Test 1 with camera rotation of 30°.

### 4.2. Test 2: Point-to-point constrained path tracking

Test 2 consisted in a point-to-point constrained path-tracking task. The trajectory to be followed was a triangular path planned as follows:

1. The end-effector had to reach the desired position $x_{sd} = [-40, 0]^T$ pixels, by starting from the initial position $x_s(0) = [0, 300]^T$ pixels, although this would be impossible because it would make contact with the wooden cube used in Test 1.

2. Once the contact occurs, the end-effector had to remain interacting with the surface of the wooden cube and arrive to $x_{sd} = [40, 0]^T$ pixels in 10 seconds, by using a linear interpolator to define intermediate points.

3. Finally, the end-effector had to return to the initial position $x_s(0)$.

In order to validate the force regulation of the proposed control scheme, in Test 2, the desired force was selected as

$$f_d = \begin{bmatrix} 0 \\ -2 \end{bmatrix} \text{N}$$

The results in Test 2 of the LPD and NLPD hybrid controllers are presented in Figures 7 and 8, respectively, and it is important to highlight some points:

- It can be observed that the position and force are correctly regulated for both controllers. Figures 7(a) and 8(a) show how, in free-space motion, the position errors tend to zero; while, during constrained motion, both error components remain constant and according with the equilibrium defined in (33). On the other hand, the force components are depicted in Figures 7(b) and 8(b), and it can be noted that both are close to zero in the absence of contact, while, during robot-environment interaction, they try to reach the desired values $[0, -2]$ N, respectively. However, in both cases for the $X$-axis component, the phenomenon of friction causes that $f_{e1} \to -0.5$ N.

- Again, it can be seen in Figure 7(c) that the control torques are more demanding in the LPD case, obtaining values closer to the limit value of 23.5 Nm. While, the 'tanh' function used in the NLPD case allows that the actuators operate in a safer operating region, as can be observed in Figure 8(c).

- The behavior of end-effector velocity is presented in Figures 7(d) and 8(d), and in both cases, it can be observed a stable response with convergence towards equilibrium (33).

Finally, it is important to note that at the start of all tests, some perturbations could be observed in the force signals (see Figures 4(b), 5(b), 6(b), 7(b) and 8(b)) and they were originated when the mechanical brake of actuators was released. Therefore, these overshoots are attributable to vibrations generated in the mechanical structure and do not represent measurements of contact forces.

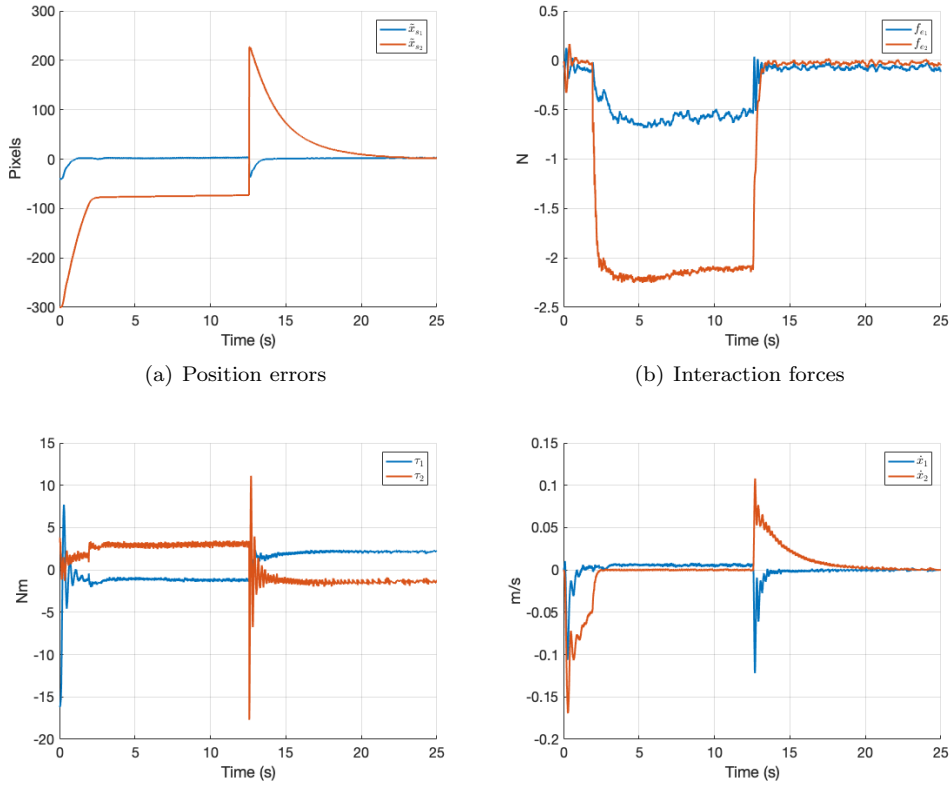


(a) Position errors

(b) Interaction forces

(c) Applied control torques

(d) End-effector velocity

**Fig. 7.** Performance of the LPD hybrid controller in Test 2.

## 5. CONCLUSIONS

In this paper, a generalised hybrid force/vision control scheme for planar robot manipulators has been presented. Multiple proportional-derivative type force/vision controllers can be derived from the proposed structure, where both force and visual data have the same level of priority, i. e. the controller tries to achieve the position-control objective as well as it exerts a desired level of force to regulate the robot-environment interaction. One of the main contributions of this work is that the proposed hybrid control structure is supported by a complete stability analysis, from which it was obtained that the equilibrium of the closed loop system is asymptotically stable in the Lyapunov sense.

The performance obtained in experimental tests, of both linear and a non-linear hybrid controllers, was satisfactory. Some of the most relevant features of the experimental responses obtained were: soft contact forces without overshoots, fast convergence of force and position error signals, robustness of the controller in the face of uncertainties such as camera rotation, operation of the robot within a safe area for its actuators when

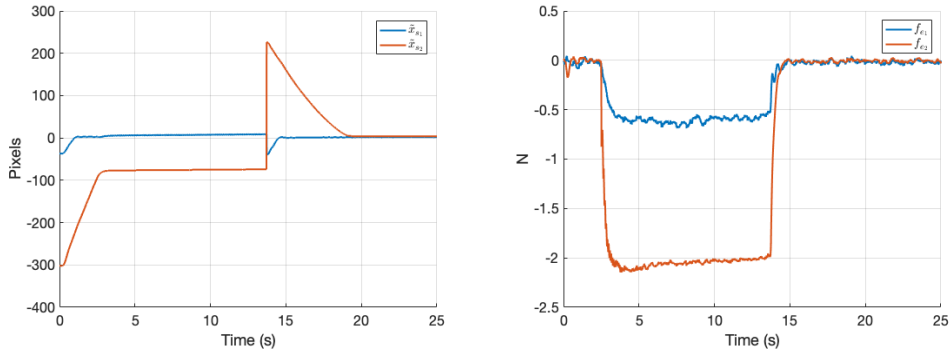


(a) Position errors




(b) Interaction forces

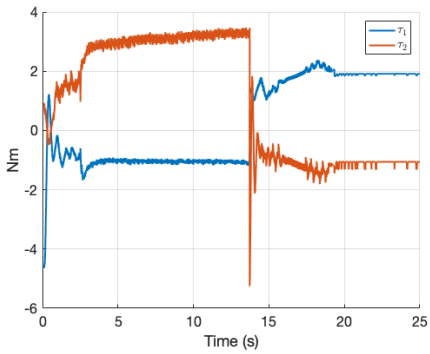


(c) Applied control torques

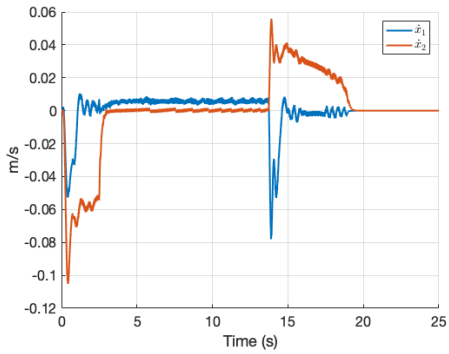


(d) End-effector velocity

**Fig. 8.** Performance of the NLPD hybrid controller in Test 2.

saturating functions are used in the mathematical structure. Additionally, because the characteristics of the hardware used in the experimental validation, it is not required the use of methods for position estimation to counteract low sampling frequencies of the vision system. However, there is the limitation that the workspace of the experimental robotic system is a plane.

As future work, it is intended to extend this proposal to the three-dimensional case. In addition, in order to have a theoretical basis of the operation of the robot in a safe area for its drive system, the problem of hybrid force/vision control of robot manipulators with bounded inputs will be addressed.

## A. TUNING PROCEDURE

The parameter/gain tuning procedure for the proposed generalised control scheme is aimed at achieving the best possible response and it is summarized in the following steps:

1. Run simulations/experiments with low control gains/coefficients. For the LPD controller (44), it is suggested to start with the following values $k_{pfj} = 0.5$, $k_{pvj} = 0.1k_{pfj}$, $k_{dj} = 10k_{pfj}$, $j = 1, \ldots, m$. While for the NLPD controller (50), it is suggested to start with the following values $k_{pfj} = k_{pvj} = k_{dj} = 0.5$, $j = 1, \ldots, m$.

2. Increase the proportional gains, $k_{pfj}$ and $k_{pvj}$, in order to reduce the rise time (speed up the closed-loop response).

3. Increase the derivative gains, $k_{dj}$, in order to reduce inertial effects, such as the overshoot.

4. Repeat steps 2 and 3 until the best possible response is obtained.

ACKNOWLEDGEMENT

This work was supported by the National Council for Science and Technology of Mexico (Grants 707604 and 707689).

(Received July 23, 2019)

REFERENCES

[1] S. Aghaie, S. Khanmohammadi, H. Moghadam-Fard, and F. Samadi: Adaptive vision-based control of robot manipulators using the interpolating polynomial. Trans. Inst. Meas. Control *36* (2014), 6, 837–844. DOI:10.1177/0142331214523307

[2] M. Bdiwi, A. Winkler, J. Suchy, and G. Zschocke: Traded and shared vision-force robot control for improved impact control. In: Proc. of the 18th IEEE International Multi-Conference on Systems, Signals and Devices, Sousse 2011, pp. 154–159. DOI:10.1109/ssd.2011.5981425

[3] R. Carelli, E. Oliva, C. Soria, and O. Nasisi: Combined force and visual control of an industrial robot. Robotica *22* (2004), 2, 163–171. DOI:10.1017/s0263574703005423

[4] C. Chávez-Olivares, F. Reyes-Cortés and E. González-Galván: On explicit force regulation with active velocity damping for robot manipulators. Automatika *56(4)* (2015), 478–490. DOI:10.1080/00051144.2015.11828661

[5] C. Chávez-Olivares, F. Reyes-Cortés, and E. González-Galván: On stiffness regulators with dissipative injection for robot manipulators. Int. J. Adv. Rob. Syst. *12* (2015), 6, 65. DOI:10.5772/60054

[6] S. Chiaverini and L. Sciavicco: The parallel approach to force/position control of robotic manipulators. IEEE Trans. Rob. Autom. *9* (1993), 4, 361–373. DOI:10.1109/70.246048

[7] P. Corke: Robotics, Vision and Control: Fundamental Algorithms in MATLAB. Springer-Verlag, London 2017. DOI:10.1007/978-3-319-54413-7

[8] N. Hogan: Stable execution of contact tasks using impedance control. In: Proc. of the IEEE International Conference on Robotics and Automation, Raleigh 1987, pp. 1047–1054. DOI:10.1109/robot.1987.1087854

[9] Y. Huang, X. Zhang, X. Chen, and J. Ota: Vision-guided peg-in-hole assembly by baxter robot. Adv. Mech. Eng. *9* (2017), 12, 168781401774807. DOI:10.1177/1687814017748078

[10] S. Hutchinson, G. D. Hager and P.I. Corke: A tutorial on visual servo control. IEEE Trans. Rob. Autom. *12* (1996), 5, 651–670. DOI:10.1109/70.538972

[11] R. Kelly: Robust asymptotically stable visual servoing of planar robots. IEEE Trans. Rob. Autom. *12* (1996), 5, 759–766. DOI:10.1109/70.538980

[12] R. Kelly, V. Santibáñez-Dávila, and J. A. Loría-Perez: Control of Robot Manipulators in Joint Space. Springer-Verlag, London 2006.

[13] X. Li, Y.H. Liu, and H. Yu: Iterative learning impedance control for rehabilitation robots driven by series elastic actuators. Automatica *90* (2018), 1–7. DOI:10.1016/j.automatica.2017.12.031

[14] V. Lippiello, B. Siciliano, and L. Villani: A position-based visual impedance control for robot manipulators. In: Proc. of the IEEE International Conference on Robotics and Automation, Roma 2007, pp. 2068–2073. DOI:10.1109/robot.2007.363626

[15] V. Lippiello, B. Siciliano, and L. Villani: Position-based visual servoing in industrial multirobot cells using a hybrid camera configuration. IEEE Trans. Rob. *23* (2007), 1, 73–86. DOI:10.1109/tro.2006.886832

[16] P. Long, W. Khalil, and P. Martinet: Robotic cutting of soft materials using force control and image moments. In: Proc. of the 13th International Conference on Control Automation Robotics and Vision, Singapore 2014, pp. 474–479. DOI:10.1109/icarcv.2014.7064351

[17] Y. Mezouar, M. Prats, and P. Martinet: External hybrid vision/force control. In: Proc. of the IEEE International Conference on Advanced Robotics, Jeju 2007, pp. 170–175.

[18] A.J. Muñoz-Vázquez, V. Parra-Vega, A. Sánchez-Orta, and F. Ruiz-Sánchez: A novel force-velocity field for object manipulation with a model-free cooperative controller. Trans. Inst. Meas. Control *41* (2019), 2, 573–581. DOI:10.1177/0142331218762272

[19] V. Mut, O. Nasisi, R. Carelli, and B. Kuchen: Tracking robust impedance robot control with visual feedback. In: Proc. of the 6th IFAC Symposium on Robot Control, Vienna 2000, pp. 69–74. DOI:10.1016/s1474-6670(17)37907-7

[20] T. Nammoto, K. Kosuge, and K. Hashimoto: Model-based compliant motion control scheme for assembly tasks using vision and force information. In: Proc. of the IEEE International Conference on Automation Science and Engineering, Wisconsin 2013, pp. 948–953. DOI:10.1109/coase.2013.6653912

[21] B. J. Nelson and P. K. Khosla: Force and vision resolvability for assimilating disparate sensory feedback. IEEE Trans. Rob. Autom. *12* (1996), 5, 714–731. DOI:10.1109/70.538976

[22] V. Ortenzi, N. Marturi, M. Mistry, J. Kuo, and R. Stolkin: Vision-based framework to estimate robot configuration and kinematic constraints. IEEE/ASME Trans. Mechatron. *23* (2018), 5, 2402–2412. DOI:10.1109/tmech.2018.2865758

[23] M. Prats, P. Martinet, A. P. Del Pobil, and S. Lee: Robotic execution of everyday tasks by means of external vision/force control. Intell. Serv. Robot. *1* (2008), 3, 253–266. DOI:10.1007/s11370-007-0008-x

[24] A. Rodriguez-Angeles and L.F. Vazquez-Chavez: Bio-inspired decentralized autonomous robot mobile navigation control for multi agent systems. Kybernetika *54* (2018), 1, 135–154. DOI:10.14736/kyb-2018-1-0135

[25] M. Takegaki and S. Arimoto: A new feedback method for dynamic control of manipulators. ASME J. Dyn. Syst. Meas. Control *103* (1981), 119–125. DOI:10.1115/1.3139651

[26] H. Wang and Y. Xie: Adaptive jacobian position/force tracking control of free-flying manipulators. Rob. Auton. Syst. *57* (2009), 2, 173–181. DOI:10.1016/j.robot.2008.05.003

[27] L. Yu, S. Fei, J. Huang, Y. Li, G. Yang, and L. Sun: Robust neural network control of robotic manipulators via switching strategy. Kybernetika *51* (2015), 2, 309–320. DOI:10.14736/kyb-2015-2-0309

[28] T. Yüksel: An intelligent visual servo control system for quadrotors. Trans. Inst. Meas. Control *41* (2019), 1, 3–13. DOI:10.1177/0142331217751599

[29] C. Zhaik: Sweep coverage of discrete time multi-robot networks with general topologies. Kybernetika *50* (2014), 1, 19–31. DOI:10.14736/kyb-2014-1-0019

*Carlos Vidrios-Serrano, Universidad Autonoma de San Luis Potosi, Facultad de Ciencias, Av. Chapultepec 1570, Privadas del Pedregal, San Luis Potosi, 78295. Mexico.*
*e-mail: cvidrios@gmail.com*

*Marco Mendoza, Universidad Autonoma de San Luis Potosi, Facultad de Ciencias, Av. Chapultepec 1570, Privadas del Pedregal, San Luis Potosi, 78295. Mexico.*
*e-mail: marco.mendoza@uaslp.mx*

*Isela Bonilla, Corresponding author. Universidad Autonoma de San Luis Potosi, Facultad de Ciencias, Av. Chapultepec 1570, Privadas del Pedregal, San Luis Potosi, 78295. Mexico.*
*e-mail: isela.bonilla@uaslp.mx*

*Berenice Maldonado-Fregoso, Universidad Autonoma de San Luis Potosi, Facultad de Ciencias, Av. Chapultepec 1570, Privadas del Pedregal, San Luis Potosi, 78295. Mexico.*
*e-mail: maldonadobere@gmail.com*